Desalination and Water Treatment
www.deswater.com
doi: 10.5004/dwt.2020.25637

189 (2020) 349–356
June

Synthesis of CdS/Nd_2S_3 nanocomposite with enhanced photocatalytic performance under simulated sunlight irradiation

Haihua Yang, Chaohua Dai, Lingjie Jiang, Li Zhang*, Jianhui Yan*

Key Laboratory of Hunan Province for Advanced Carbon-based Functional Materials, School of Chemistry and Chemical Engineering, Hunan Institute of Science and Technology, Yueyang, Hunan 414006, PR China, Tel. +86 7308640122; emails: hgx.zl@163.com (L. Zhang), yanjh58@163.com (J. Yan), hhyang@126.com (H. Yang), dai353009459@163.com (C. Dai), 554136209@qq.com (L. Jiang)

Received 19 August 2019; Accepted 6 February 2020

ABSTRACT

The synthesis of CdS/Nd_2S_3 nanocomposite photocatalysts was conducted via a solvothermal process followed by a post calcination treatment. The phase structures, composition, morphologies and light absorption properties of the samples were analyzed by X-ray diffraction, scanning electron microscopy, energy-dispersive X-ray spectroscopy, transmission electron microscopy, high-resolution transmission electron microscopy, Brunauer–Emmett–Teller and UV-Vis diffuse reflectance spectra techniques. The characterization results indicate that the CdS/Nd_2S_3 nanocomposite possesses good crystallinity, small particle size and strong simulated sunlight absorption. This nanocomposite is found to be effective for the photocatalytic degradation of methyl orange under simulated sunlight irradiation. The maximum photocatalytic degradation rate of 96.3% obtained over the CdS/Nd_2S_3 nanocomposite is 1.77 and 3.90 times higher than that of CdS and Nd_2S_3, respectively. As investigated by photocurrent measurement and photoluminescence spectroscopy, remarkable enhanced photogenerated charge separation is achieved by the CdS/Nd_2S_3 nanocomposite. A type-II band alignment is proposed to elucidate the photocatalytic mechanism within the nanocomposite.

Keywords: CdS; Nd_2S_3; Nanocomposite; Solvothermal method; Photocatalytic degradation; Simulated sunlight irradiation

1. Introduction

Energy crisis and environmental pollution are arising as the most urgent issues. It is of great significance to develop new and efficient technologies to solve these problems. Among the numerous proposed strategies, semiconductor photocatalysts have been recognized as one of the most efficient and environmental-friendly technologies in the near future [1–4]. With the irradiation of sunlight, the semiconductor photocatalysts are excited and generate electrons and holes, which can be utilized for energy conversion or degradation of organic pollutants [5–7]. The efficiency and practicability of photocatalytic degradation dominantly depend on the semiconductor photocatalysts, which should own suitable energy band alignment for efficient sunlight absorption, rapid separation of photogenerated electron-hole pairs, as well as low cost. Various semiconductor photocatalysts, such as TiO_2 [8,9], ZnO [10,11], Bi_2WO_6 [12], C_3N_4 [7,13], etc., have been explored to fulfill the requirements.

Due to their narrow band gaps, metal sulfides have attracted intensive attention for photocatalytic hydrogen production and organic pollutant degradation [14–18]. Typically, cadmium sulfide (CdS) is a direct band gap semiconductor with a narrow band gap of 2.4 eV, which can absorb sunlight irradiation with wavelengths up to 516 nm [5,19–21]. It is worth mentioning that because CdS possesses appropriate conductive band (CB) edge (–0.5 eV vs. NHE) and valence band (VB) position (1.9 eV vs. NHE), the photogenerated electrons are capable of reducing the adsorbed O_2 or other oxidizing substances to yield

* Corresponding authors.

superoxide radicals ($^{\bullet}O_2^-$), and further form hydroxyl radicals ($^{\bullet}OH$) [5,22]. The $^{\bullet}O_2^-$ and $^{\bullet}OH$ radicals, together with the photogenerated holes, have high oxidation ability and can efficiently oxidize various organic dyes and contaminants. However, the rapid electron-hole recombination and photocorrosion are the most common shortcomings of bulk CdS photocatalyst. Different kinds of methods have been proposed to boost the photocatalytic performance of CdS. Preparation of CdS with nanostructures and morphologies can expose more active sites, promote separation of electro-hole pairs, and shorten the diffusion distance, and thus improve the photocatalytic activity [23–27]. It also has been revealed that composite materials based on CdS nanostructures and conductive platforms (such as activated carbon, porous carbon, or nitrogen-doped carbon) display excellent photocatalytic efficiency, which is largely due to the synergistically enhanced solar energy harvesting efficiency and electron-hole separation [28–32]. Combining CdS with other semiconductors to construct nanostructured heterojunction photocatalysts has also been proved as an attractive strategy to broaden the visible light absorption, accelerate the separation of photogenerated carriers, and provide with rich active sites for degradation of organic contaminants [33–36]. For instance, nanocomposites of CdS nanoparticles, nanowires, or porous nanostructures with $BiVO_4$ and/or Ag have been certified as photocatalysts with excellent photocatalytic performance and durability [22,37–39]. As a rare-earth sulfide, neodymium sesquisulfide (Nd_2S_3) shows excellent thermoelectric, optical, luminescence, electro-optical and magneto-optical properties [40–44]. Nd_2S_3 possesses a bandgap of 2.7 eV, and the CB and VB edges locate at –1.2 and 1.5 eV vs. NHE, respectively. [45,46]. However, to the best of our knowledge, no research has been reported about the photocatalytic performance of Nd_2S_3.

Inspired by the progress and growing interest of metal sulfides based composites for photocatalytic degradation of organic pollutants, herein two-component CdS/Nd_2S_3 nanocomposite has been synthesized and exhibits remarkably enhanced photocatalytic performance for the degradation of methyl orange (MO). Based on the difference of energy bands between CdS and Nd_2S_3, a type-II band alignment is built within the heterojunction. The photogenerated electrons produced by Nd_2S_3 can be transferred to the CB of CdS, and the holes tend to move from the VB of CdS to that of Nd_2S_3, so as to accelerate the separation of photogenerated electron-hole pairs and interfacial charge transport within the heterojunction nanocomposite, and thus improve the photocatalytic activity. This work is expected to enhance the photocatalytic performance of CdS, and enlarge the practical applications of Nd_2S_3.

2. Materials and methods

2.1. Synthesis of CdS/Nd_2S_3 nanocomposite

All chemicals were of analytical grade and employed without further purification. CdS/Nd_2S_3 nanocomposite was synthesized via a solvothermal process followed by a post calcination treatment. 5 mmol of cadmium nitrate ($Cd(NO_3)_2{\cdot}4H_2O$) and 10 mmol of neodymium nitrate ($Nd(NO_3)_3{\cdot}6H_2O$) was dissolved in 80 mL of ethylene glycol to form solution A with a 1:2 molar ratio of Cd/Nd. 30 mmol of thioacetamide (TAA, CH_3CSNH_2) was added to 40 mL of ethylene glycol to get solution B. Solution B was slowly dropped into solution A under vigorous stirring, and any other dissolved gases were removed by continuous purging with nitrogen. The mixed solution was then transferred into Teflon-lined autoclave, and heated at 140°C for 24 h. The as-obtained precipitates were centrifuged and washed with deionized water, followed by drying at 60°C for 12 h to get the precursor, which was finally calcined at 400°C for 2 h in a nitrogen atmosphere to obtain the CdS/Nd_2S_3 nanocomposite (denoted as Cd-Nd-S-2). For comparison, bare CdS, Nd_2S_3, and CdS/Nd_2S_3 nanocomposites with initial Cd/Nd molar ratios of 1:1 and 1:3 (defined as Cd-Nd-S-1 and Cd-Nd-S-3, respectively) were fabricated with the same procedure.

2.2. Characterization

Powder X-ray diffraction (XRD) was performed on a Bruker D8 Advance X-ray diffractometer under Cu Kα radiation (λ = 1.5418 Å) at a voltage of 40 kV and a current of 40 mA. The morphology and elemental composition were observed by scanning electron microscope (SEM, Nova Nano230) with an energy-dispersive X-ray spectroscopy (EDS) detector, transmission electron microscope (TEM) and high-resolution transmission electron microscope (HRTEM, JEOL, Tokyo, Japan JEM–2010). UV-vis diffuse reflectance spectra of the samples were characterized using a UV-vis spectrophotometer (UV-2550, Shimadzu, Japan). $BaSO_4$ was employed as the reflectance standard in the UV-vis diffuse reflectance experiment. The Brunauer–Emmett–Teller (BET) specific surface area and the pore structure characteristics were determined by a nitrogen adsorption–desorption isotherm apparatus (ST–08 analyzer). The photoluminescence (PL) spectra were investigated on an Agilent G9800A (California, USA) spectrophotometer with the excitation wavelength at 400 nm.

2.3. Photocatalytic activity evaluation

The photocatalytic degradation activity of the as-prepared catalysts was evaluated by the degradation of methyl orange (MO). 0.2 g of photocatalyst powder was sonicated and dispersed in 100 mL of MO dye solution (25 mg L^{-1}) and magnetically stirred in dark for 30 min to reach adsorption/desorption equilibrium. A 150 W Xenon lamp was used as the simulated sunlight source with wavelengths ranging from 200 to 900 nm. During the irradiation, the catalyst particles were kept in suspension state by magnetic stirring. At regular intervals of 10 min, 2 mL of the suspension was extracted and centrifuged. the concentration of MO was measured by a UV-2600 (Shimadzu, Japan) spectrophotometer at the characteristic wavelength (465 nm). The degradation rate was presented as C/C_0, where C_0 and C were the initial concentration of MO and the time-dependent concentration of MO upon irradiation, respectively. Total organic carbon (TOC) analysis was carried out with a Shimadzu, Japan, 5000A TOC analyzer. After the photocatalysis, the used catalyst powder was washed with deionized water and collected for the recycling test under the same measurement condition. Each set of photocatalytic measurements was repeated three times to control the experimental error within ±5%.

The transient photocurrent of the samples was recorded on an electrochemical workstation (CHI 660E) with a classic three-electrode system. Pt plate and Ag/AgCl were used as a counter electrode and a reference electrode, respectively. 20 mg of the photocatalyst was dispersed in 20 mL of ethanol and dropcasted onto F-doped SnO_2-coated glass (FTO glass, 1 cm × 1 cm). The electrolyte was 0.1 M sodium sulfate aqueous solution. A 300 W Xenon lamp was used as the light source. The photocurrent response (I-t) was measured with a voltage bias of 1.8 V.

3. Results and discussion

3.1. Characterization of the photocatalysts

Fig. 1 shows the XRD patterns of CdS, Nd_2S_3 and Cd-Nd-S-2 nanocomposite. The diffraction peaks of CdS sample are of high intensity and match well with the hexagonal CdS phase (JCPDS No. 01-089-2944) and cubic CdS phase (JCPDS No. 01-089-0440) [28,47], indicating the as-obtained CdS is of high crystallinity. For Nd_2S_3 sample, only one diffraction peak at 25.6° with low intensity can be ascribed to the (211) crystal plane of cubic Nd_2S_3 phase (JCPDS No. 26-1450), implying its poor crystallinity [46]. The uncalcined Cd-Nd-S-2 precursor shows the same XRD peaks position as that of CdS, but the weaker intensity indicates its lower crystallinity. The diffraction peaks of the Cd-Nd-S-2 sample become stronger upon further calcination, suggesting its improved crystallinity. By taking a close look, the diffraction peak of the (002) crystal plane of CdS becomes broaden because of the incorporation of the (211) crystal plane of cubic Nd_2S_3 in the nanocomposite.

The micromorphology and composition of the as-prepared samples were identified by SEM, EDS, TEM and HRTEM (Fig. 2). As presented in Fig. 2a, the as-synthesized CdS sample is composed of microspheres with different particle sizes. Fig. 2b reveals that the Nd_2S_3 sample consists of irregular nanoparticles, which partially agglomerate with each other. As shown in Fig. 2c and e, the Cd-Nd-S-2 nanocomposite also shows irregular nanostructure similar to the Nd_2S_3 sample, but the physical agglomeration is largely alleviated. The EDS elemental mapping images of the Cd-Nd-S-2 nanocomposite (Fig. 2d) reveal that Cd, Nd and S elements are uniformly distributed in the final product. The atomic contents of Cd, Nd and S elements in different samples are determined by EDS and summarized as shown in Table 1. The HRTEM image of the Cd-Nd-S-2 nanocomposite displays clear lattice fringes (Fig. 2f). The resolved d spacing of 0.338 nm can be indexed to the (002) and (111) crystal plane of hexagonal and cubic CdS, respectively [28,47]. The lattice spacing of 0.358 nm corresponds to the (100) crystal planes of hexagonal CdS, respectively, while the *d* spacing of 0.346 nm matches well with the (211) crystal plane of cubic Nd_2S_3. The aforementioned results certify the successful construction of CdS/Nd_2S_3 nanocomposite.

N_2 adsorption–desorption isotherm measurements are conducted to further investigate the BET specific surface area of the samples. As presented in Table 1 and Fig. 3, CdS shows the lowest specific surface area, while Nd_2S_3 sample and Cd-Nd-S-2 nanocomposite depict a much larger specific surface area, which is attributed to their smaller nanoparticles. Larger specific surface area is propitious to the adsorption of the organic pollutant, rapid photocatalytic reaction, and desorption of the product molecules, and thus better photocatalytic activity [48].

The optical absorption property is essential for the photocatalytic performance of semiconductor photocatalysts, and it can be characterized by UV–vis absorption spectra. As shown in Fig. 4, Nd_2S_3 exhibits negligible absorption in both UV and visible light regions, which may be due to its low crystallinity. Both of CdS and Cd-Nd-S-2 samples display similar absorption edges located at around 540 nm, suggesting good visible light absorption. It is interesting to observe a pronounced enhancement of light absorption intensity after the integration of Nd_2S_3 and CdS to form Cd-Nd-S-2 nanocomposite, which would play an essential role in photocatalytic reaction [49]. The inset shows the corresponding Kubleka–Munk plots, and the bandgaps of CdS and Cd-Nd-S-2 are determined as 2.27 and 2.31 eV [22,27,37,38].

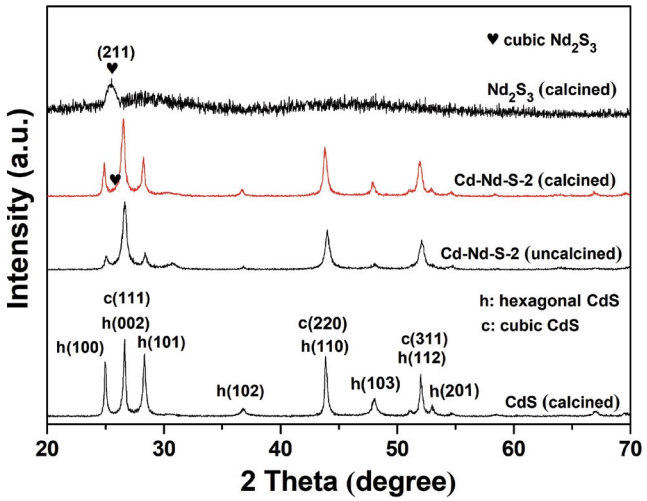

Fig. 1. XRD patterns of CdS, Nd_2S_3, uncalcined and calcined Cd-Nd-S-2 nanocomposites.

3.2. Photocatalytic activity

The photocatalytic behaviors of different catalysts were evaluated with MO as the model organic pollutant. As elucidated in Fig. 5a, no obvious MO concentration change was observed in the first 30 mins without light illumination for all of these photocatalysts, implying low physical adsorption ability, which might be due to the low specific surface area. Nd_2S_3 alone does not show obvious photocatalytic degradation of MO, while the photocatalytic activity of CdS is superior to Nd_2S_3. It can be explained by the crystallinity, specific surface area, light absorption ability and photogenerated electron-holes separation. Although a larger specific surface area is observed for bare Nd_2S_3, the lower crystallinity and weak light absorption account for the lowest photocatalytic degradation rate (24.7%). The high crystallinity is a favorable factor to obtaining a higher photocatalytic degradation rate (54.2%) on bare CdS. It should be mentioned that the rapid photogenerated electrons and holes recombination is the bottleneck for the photocatalytic

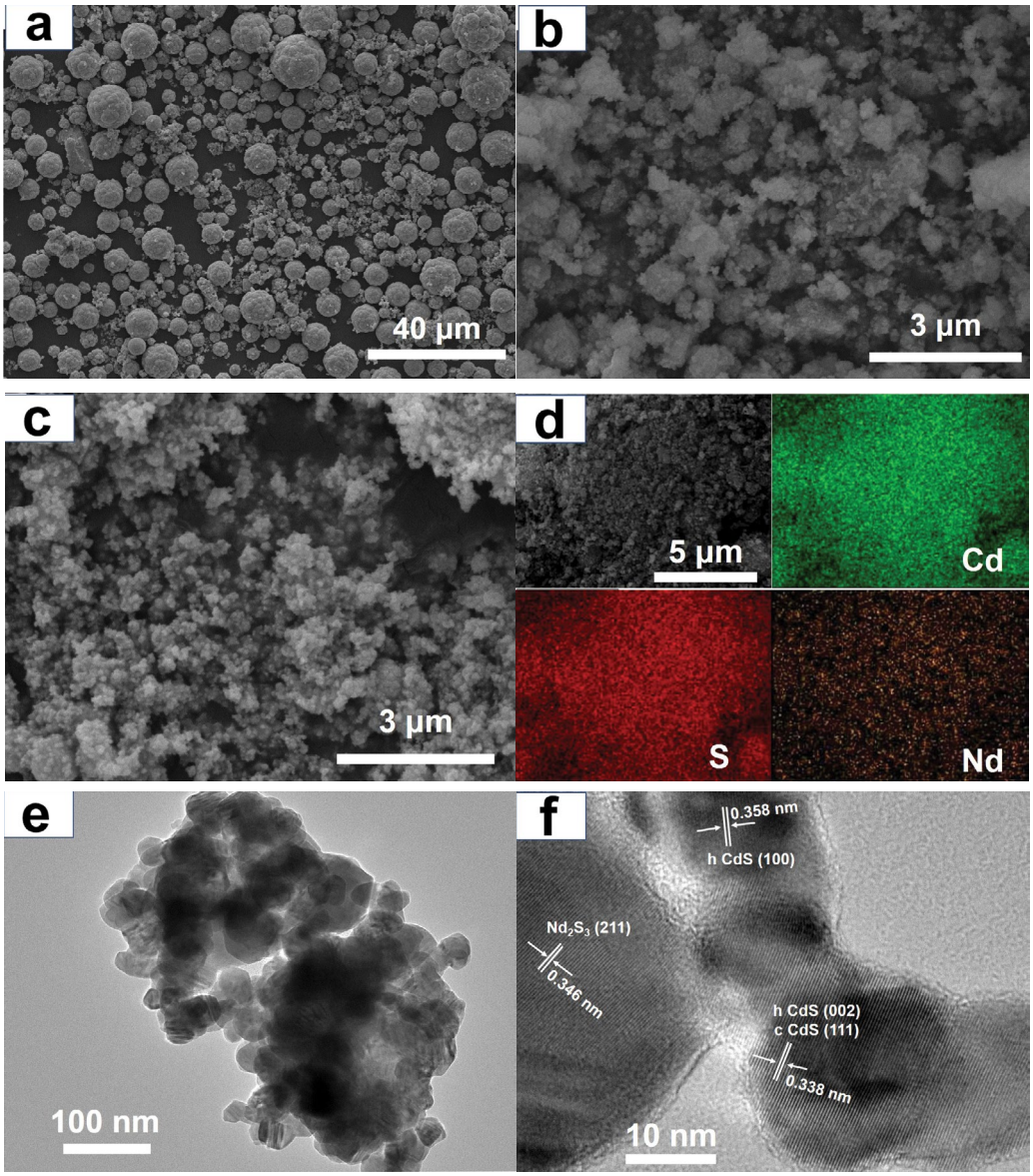

Fig. 2. SEM images of (a) CdS, (b) Nd_2S_3, (c) SEM image, (d) elemental mapping, (e) TEM image and (f) HRTEM image of Cd-Nd-S-2 nanocomposite.

Table 1
Atomic contents of Cd, Nd, and S elements, and BET surface area of the as-prepared samples

Sample	Cd (atomic%)	Nd (atomic%)	S (atomic%)	S_{BET} (m^2 g^{-1})
CdS	49.7	0	50.3	13
Cd-Nd-S-1	39.2	8.1	52.7	/
Cd-Nd-S-2	26.9	17.9	55.2	21
Nd_2S_3	0	39.1	60.9	22

activity of bare CdS. It has been reported that construction of heterojunction nanocomposites could accelerate the separation and transport of photogenerated electrons and holes, which would promote the photocatalytic efficiency [12,18,22,27,37,38]. This fact is further demonstrated by the construction of CdS/Nd_2S_3 nanocomposites. Notably the photocatalytic performances increase as the integration of CdS and Nd_2S_3 to construct CdS/Nd_2S_3 nanocomposites. Among the nanocomposites, the Cd-Nd-S-2 photocatalyst displays the best performance, manifesting that an optimal

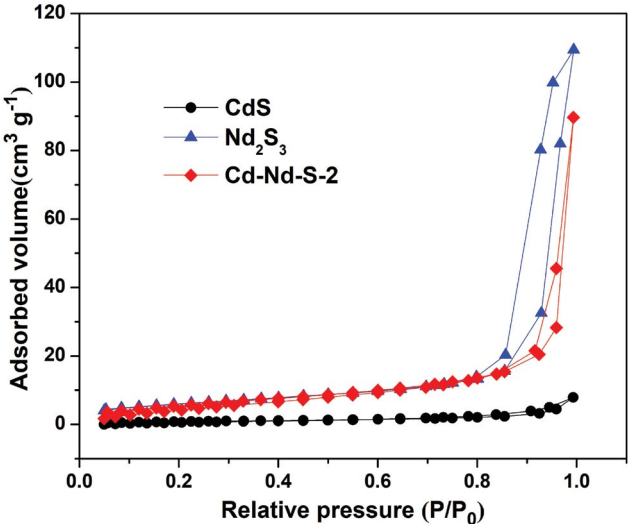

Fig. 3. BET adsorption–desorption isotherms of (a) CdS, (b) Nd_2S_3, and (c) Cd-Nd-S-2.

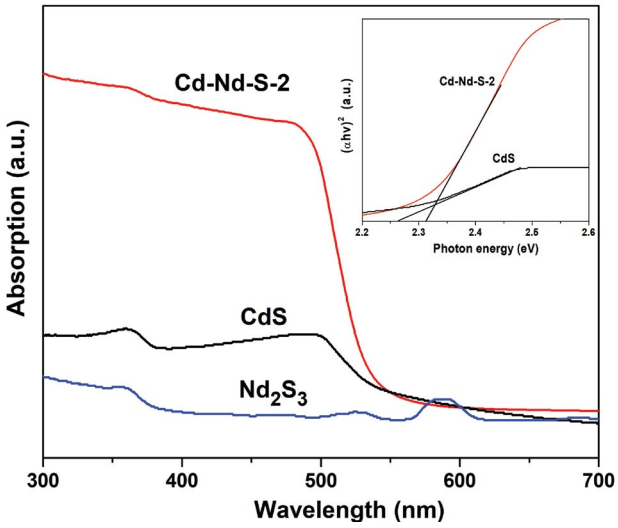

Fig. 4. UV-vis diffraction reflection spectra of CdS, Nd_2S_3 and Cd-Nd-S-2 nanocomposite.

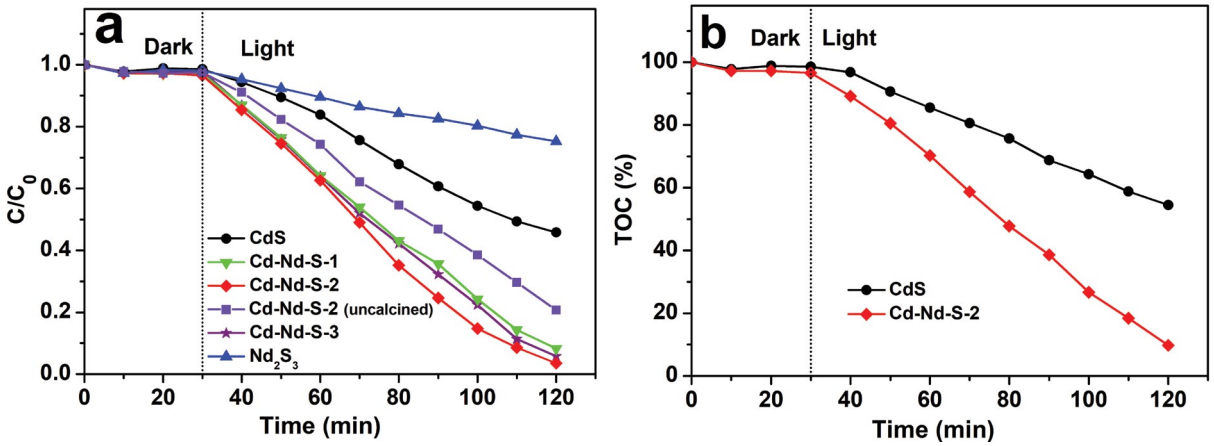

Fig. 5. (a) Photocatalytic performances of the as-prepared photocatalysts and (b) total organic carbon (TOC %) during the photocatalytic process by CdS and Cd-Nd-S-2 photocatalysts.

synergistic interaction between CdS and Nd_2S_3 is required for achieving the highest photocatalytic activity. The uncalcined Cd-Nd-S-2 photocatalyst shows inferior photocatalytic performance to the calcined one, which is consistent with the lower crystallinity of the Cd-Nd-S-2 precursor as shown in XRD results. In order to confirm whether only decolorization or mineralization of MO dye occurs during the photocatalytic process, the TOC removal efficiencies by CdS and Cd-Nd-S-2 photocatalysts were investigated at regular intervals of illumination (Fig. 5b). It is found that the mineralization of MO takes place gradually as the photocatalytic reaction going on. However, the mineralization of MO is slower than the degradation process, and more time is required to achieve a desirable removal of TOC.

Besides the photocatalytic activity, stability is also of great significance to the practical application of photocatalysts. Therefore, recycling experiments were conducted to verify the photocatalytic stability of the Cd-Nd-S-2 nanocomposite. As shown in Fig. 6, the photocatalytic activity of Cd-Nd-S-2 is still of high level under continuous irradiation for several runs, and no obvious fading of photocatalytic activity is observed after six successive recycles, suggesting good stability during the photocatalytic process.

In order to get insight into the separation and transfer of photogenerated electron-hole pairs, photoluminescence (PL) and transient photocurrents of the as-obtained samples were measured as shown in Fig. 7. It's well known that PL originates from the recombination of photogenerated electrons and holes, while lower PL intensity may imply a more efficient separation of photogenerated electron-hole pairs [37,38]. As shown in Fig. 7a, the CdS sample exhibits the strongest PL intensity, revealing the high recombination rate of photogenerated electron-hole pairs. The Nd_2S_3 sample displays negligible PL intensity, which is consistent with its low crystallinity and UV-vis light absorption. The PL intensities fall off by the involvement of Nd_2S_3 in CdS to form

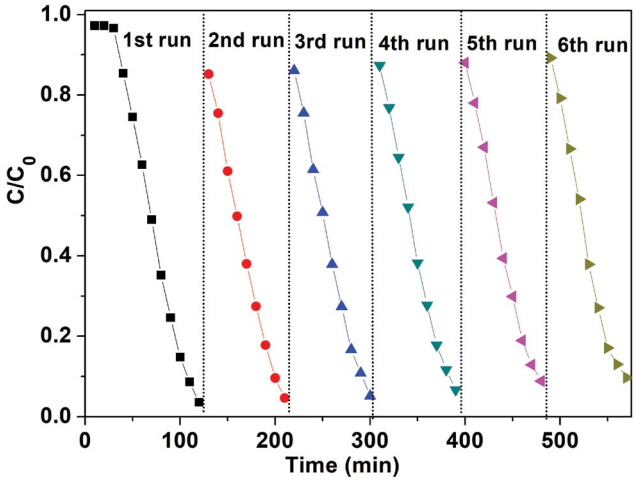

Fig. 6. Recycling tests of Cd-Nd-S-2 photocatalyst for photocatalytic degradation of MO.

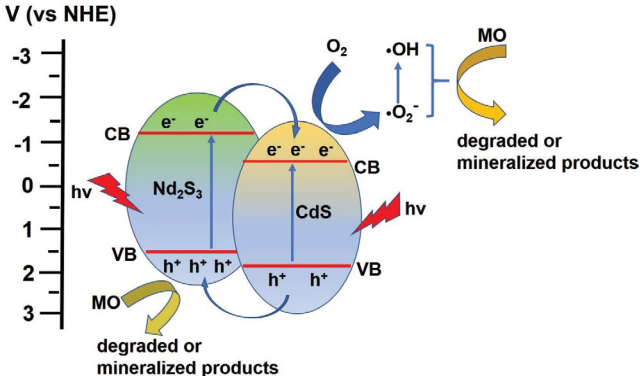

Fig. 8. Schematic illustration of the proposed mechanism toward photodegradation of MO over CdS/Nd_2S_3 nanocomposite.

nanocomposites, typically for Cd-Nd-S-2, demonstrating the recombination of photogenerated electron-hole pairs is efficiently suppressed. Moreover, the transient photocurrents are collected to reflect the photogenerated charges separation and transfer [37,38,50,51]. Similar to the previous reports, the photocurrent of Cd-Nd-S-2 nanocomposite is much higher than that of CdS and Nd_2S_3. It means that the construction of nanocomposite promotes the separation of photogenerated carriers, which further transfer to the collecting electrode and contribute to the higher photocurrent.

Based on the aforementioned results and discussion, a possible mechanism is proposed to elucidate the photocatalytic degradation of MO by CdS/Nd_2S_3 nanocomposite. As illustrated in Fig. 8, the CB edge of Nd_2S_3 locates at –1.2 eV, more negative than that of CdS, while the VB edge of Nd_2S_3 is 1.5 eV, less positive than that of CdS, implying that Nd_2S_3 and CdS fit the requirements to form a type-II heterojunction with well-matched band structures [5,22,45,46]. Under the simulated sunlight irradiation, the photogenerated electrons migrate from the CB of Nd_2S_3 to the CB of CdS. At the same time, the holes on the VB of CdS move to the VB of Nd_2S_3. As a result, it reduces the probability of electron-hole pairs recombination, and make the charges separation more efficiently. Furthermore, the electrons on the CB of CdS are capable of reducing O_2 to produce $^{\bullet}O_2^-$ and finally $^{\bullet}OH$ radicals [5,22,38]. The as generated holes, $^{\bullet}O_2^-$ and $^{\bullet}OH$ radicals have strong oxidative activity, and can quickly oxidize MO dye. In short, the type-II CdS/Nd_2S_3 heterojunction boosts the separation and transfer of the electron-hole pairs and greatly promotes the photocatalytic performance.

4. Conclusions

In summary, CdS/Nd_2S_3 nanocomposite photocatalyst has been prepared via a solvothermal process followed by a post calcination treatment. As compared to CdS and Nd_2S_3, the as-prepared CdS/Nd_2S_3 nanocomposite displays significantly enhanced photocatalytic activity toward degradation of MO under simulated sunlight irradiation. The greatly enhanced photocatalytic activity of CdS/Nd_2S_3 nanocomposite is dominantly ascribed to the type-II band alignment within the nanocomposite, which accelerates the separation and transfer of photogenerated electron-hole pairs. This

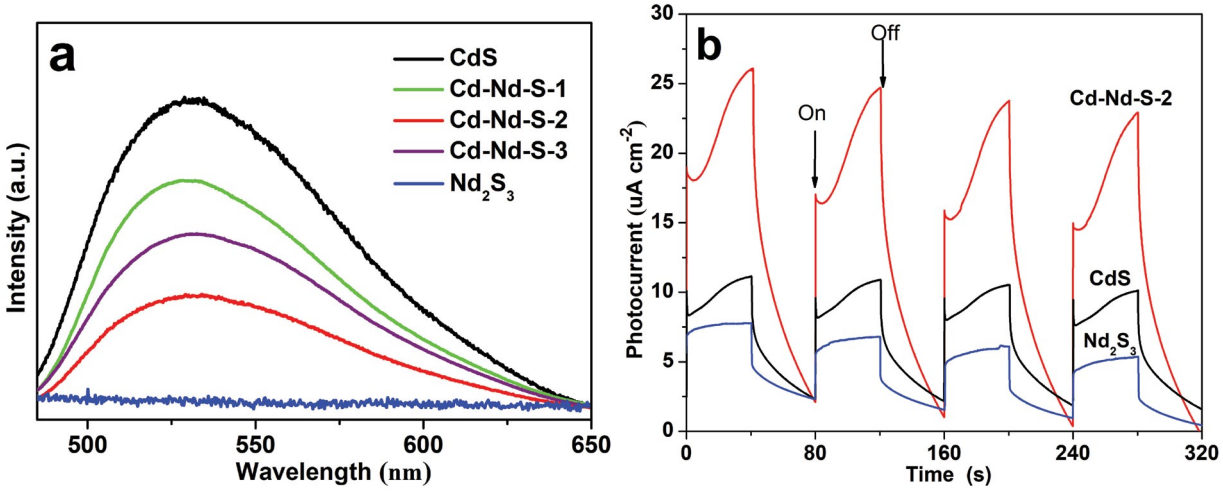

Fig. 7. (a) Photoluminescence spectra and (b) transient photocurrent-time (I-t) curves of the as-obtained samples.

work provides a feasible way to enhance improve the photocatalytic performance of CdS and enrich the application area of Nd_2S_3.

Acknowledgments

This research was financially supported by the Natural Science Foundation for Youths of Hunan Province of China (No. 2019JJ50206), the Innovation Platform Foundation Project of Hunan Provincial Education Department of China (No. 18K087), and Research-based Learning and innovative Experimental Program for College students of Hunan Province (No. S201912658002).

References

[1] C.S. Turchi, D.F. Ollis, Photocatalytic degradation of organic water contaminants: mechanisms involving hydroxyl radical attack, J. Catal., 122 (1990) 178–192.
[2] M.A. Meetani, A. Alaidaros, S. Hisaindee, A. Alhamadat, R. Selvaraj, F. Al Marzouqi, M.A. Rauf, Photocatalytic degradation of acetaminophen in aqueous solution by $Zn_{0.2}Cd_{0.8}S$ catalyst and visible radiation, Desal. Water Treat., 138 (2019) 270–279.
[3] L. Daneshvar, A. Nezamzadeh-Ejhieh, Photocatalytic activity of ZnO nanoparticles towards tinidazole degradation: experimental design by response surface methodology (RSM), Desal. Water Treat., 141 (2019) 364–376.
[4] A. Rahmani, H. Rahimzadeh, S. Beirami, Photocatalytic degradation of phenolic compound (Phenol, resorcinol, and cresol) by titanium dioxide photocatalyst on ordered mesoporous carbon (CMK-3) support under UV irradiation, Desal. Water Treat., 144 (2019) 224–232.
[5] L. Cheng, Q. Xiang, Y. Liao, H. Zhang, CdS-Based photocatalysts, Energy Environ. Sci., 11 (2018) 1362–1391.
[6] N. Jiang, Z. Xiu, Z. Xie, H. Li, G. Zhao, W. Wang, Y. Wu, X. Hao, Reduced graphene oxide–CdS nanocomposites with enhanced visible-light photoactivity synthesized using ionic-liquid precursors, New J. Chem., 38 (2014) 4312–4320.
[7] J. Fu, B. Chang, Y. Tian, F. Xi, X. Dong, Novel C_3N_4–CdS composite photocatalysts with organic–inorganic heterojunctions: in situ synthesis, exceptional activity, high stability and photocatalytic mechanism, J. Mater. Chem. A, 1 (2013) 3083–3090.
[8] I.K. Konstantinou, T.A. Albanis, TiO_2-assisted photocatalytic degradation of azo dyes in aqueous solution: kinetic and mechanistic investigations: a review, Appl. Catal., B, 49 (2004) 1–14.
[9] Z. Yi, Y. Zeng, H. Wu, X. Chen, Y. Fan, H. Yang, Y. Tang, Y. Yi, J. Wang, P. Wu, Synthesis, surface properties, crystal structure and dye-sensitized solar cell performance of TiO_2 nanotube arrays anodized under different parameters, Results Phys., 15 (2019) 102609.
[10] Z. Yi, X. Li, H. Wu, X. Chen, H. Yang, Y. Tang, Y. Yi, J. Wang, P. Wu, Fabrication of ZnO@Ag_3PO_4 core-shell nanocomposite arrays as photoanodes and their photoelectric properties, Nanomaterials, 9 (2019) 1254.
[11] L. Zhang, Q. Liang, P. Yang, Y. Huang, Y. Liu, H. Yang, J. Yan, ZIF-8 derived ZnO/$Zn_6Al_2O_9$/Al_2O_3 nanocomposite with excellent photocatalytic performance under simulated sunlight irradiation, New J. Chem., 43 (2019) 2990–2999.
[12] S. Wang, H. Yang, Z. Yi, X. Wang, Enhanced photocatalytic performance by hybridization of Bi_2WO_6 nanoparticles with honeycomb-like porous carbon skeleton, J. Environ. Manage., 248 (2019) 109341.
[13] X. Wang, M. Hong, F. Zhang, Z. Zhuang, Y. Yu, Recyclable nanoscale zero-valent iron-doped g-C_3N_4/MoS_2 for efficient photocatalysis of RhB and Cr(VI) driven by visible light, ACS Sustainable Chem. Eng., 4 (2016) 4055–4063.
[14] M. Kaur, S.K. Mehta, S.K. Kansal, Visible light-driven photocatalytic degradation of ofloxacin and malachite green dye using cadmium sulfide nanoparticles, J. Environ. Chem. Eng., 6 (2018) 3631–3639.
[15] Y. Chen, Y. Liang, T. Li, C. Lin, L. Lin, M. Zhao, Y. Wang, H. Chen, J. Zeng, Y. Zhang, Hydrothermal fabrication of sandwich-structured silver sulfide/ferroferric oxide/silver metavanadate graphene microtube using capillary effect for enhancing photocatalytic degradation and disinfection, J. Colloid Interface Sci., 555 (2019) 759–769.
[16] M. Jourshabani, Z. Shariatinia, G. Achari, C.H. Langford, A. Badiei, Facile synthesis of NiS_2 nanoparticles ingrained in a sulfur-doped carbon nitride framework with enhanced visible-light photocatalytic activity: two functional roles of thiourea, J. Mater. Chem. A, 6 (2018) 13448–13466.
[17] T. Di, Q. Xu, W. Ho, H. Tang, Q. Xiang, J. Yu, Review on metal sulfide-based Z-scheme photocatalysts, ChemCatChem, 11 (2019) 1394–1411.
[18] H.-B. Huang, K. Yu, J.-T. Wang, J.-R. Zhou, H.-F. Li, J. Lü, R. Cao, Controlled growth of ZnS/ZnO heterojunctions on porous biomass carbons via one-step carbothermal reduction enables visible-light-driven photocatalytic H_2 production, Inorg. Chem. Front., 6 (2019) 2035–2042.
[19] R. Jiang, J. Yao, H. Zhu, Y. Fu, Y. Guan, L. Xiao, G. Zeng, Effective decolorization of congo red in aqueous solution by adsorption and photocatalysis using novel magnetic alginate/γ-Fe_2O_3/CdS nanocomposite, Desal. Water Treat., 52 (2014) 238–247.
[20] L. Yu, Y. Tang, X. Liu, C. Ma, P. Huo, J. Pan, W. Shi, Y. Yan, Hydrothermal synthesis of the cauliflower-like CdS microspheres to enhance solar photocatalytic degradation of oxytetracycline hydrochloride, Desal. Water Treat., 55 (2015) 2144–2154.
[21] H.R. Pouretedal, S.D. Mirghaderi, M.H. Keshavarz, Decolorization kinetic studies of congo red catalyzed by Co-doped CdS nanoparticles, Desal. Water Treat., 20 (2010) 220–227.
[22] L. Zou, H. Wang, X. Wang, High efficient photodegradation and photocatalytic hydrogen production of CdS/$BiVO_4$ heterostructure through Z-scheme process, ACS Sustainable Chem. Eng., 5 (2017) 303–309.
[23] Y.V. Marathe, M.M.V. Ramanna, V.S. Shrivastava, Synthesis and characterization of nanocrystalline CdS thin films grown by chemical bath deposition at different molarities for removal of methylene blue, Desal. Water Treat., 51 (2013) 5813–5820.
[24] S. Shenoy, E. Jang, T.J. Park, C.S. Gopinath, K. Sridharan, Cadmium sulfide nanostructures: influence of morphology on the photocatalytic degradation of erioglaucine and hydrogen generation, Appl. Surf. Sci., 483 (2019) 696–705.
[25] K. Wu, Z. Chen, H. Lv, H. Zhu, C.L. Hill, T. Lian, Hole removal rate limits photodriven H_2 generation efficiency in CdS-Pt and CdSe/CdS-Pt semiconductor nanorod–metal tip heterostructures, J. Am. Chem. Soc., 136 (2014) 7708–7716.
[26] Y. Ben-Shahar, F. Scotognella, I. Kriegel, L. Moretti, G. Cerullo, E. Rabani, U. Banin, Optimal metal domain size for photocatalysis with hybrid semiconductor-metal nanorods, Nat. Commun., 7 (2016) 10413.
[27] N. Bao, L. Shen, T. Takata, K. Domen, Self-templated synthesis of nanoporous CdS nanostructures for highly efficient photocatalytic hydrogen production under visible light, Chem. Mater., 20 (2008) 110–117.
[28] H.-B. Huang, Y. Wang, W.-B. Jiao, F.-Y. Cai, M. Shen, S.-G. Zhou, H.-L. Cao, J. Lü, R. Cao, Lotus-leaf-derived activated-carbon-supported nano-CdS as energy-efficient photocatalysts under visible irradiation, ACS Sustainable Chem. Eng., 6 (2018) 7871–7879.
[29] H.-B. Huang, Y. Wang, F.-Y. Cai, W.-B. Jiao, N. Zhang, C. Liu, H.-L. Cao, J. Lü, Photodegradation of rhodamine B over biomass-derived activated carbon-supported CdS nanomaterials under visible irradiation, Front. Chem., 5 (2017) 00123, doi: 10.3389/fchem.2017.00123.
[30] H.-L. Cao, F.-Y. Cai, K. Yu, Y.-Q. Zhang, J. Lü, R. Cao, Photocatalytic degradation of tetracycline antibiotics over CdS/nitrogen-doped–carbon composites derived from in situ carbonization of metal–organic frameworks, ACS Sustainable Chem. Eng., 7 (2019) 10847–10854.
[31] J.-Y. Yu, Z.-J. Chen, X.-Y. Zeng, C. Liu, F.-Y. Cai, H.-L. Cao, J. Lü, Morphological control of CdS@AC nanocomposites for

enhanced photocatalytic degradation of tetracycline antibiotics under visible irradiation, Inorg. Chem. Commun., 95 (2018) 134–138.
[32] H.-B. Huang, N. Zhang, K. Yu, Y.-Q. Zhang, H.-L. Cao, J. Lü, R. Cao, One-step carbothermal synthesis of robust CdS@BPC photocatalysts in the presence of biomass porous carbons, ACS Sustainable Chem. Eng., 7 (2019) 16835–16842.
[33] Y.V. Marathe, V.S. Shrivastava, Effective removal of non-biodegradable methyl orange dye by using CdS/activated carbon nanocomposite as a photocatalyst, Desal. Water Treat., 53 (2015) 1316–1323.
[34] W. Xing, L. Ni, X. Liu, Y. Luo, Z. Lu, Y. Yan, P. Huo, Effect of metal ion (Zn^{2+}, Bi^{3+}, Cr^{3+}, and Ni^{2+})-doped CdS/halloysite nanotubes (HNTs) photocatalyst for the degradation of tetracycline under visible light, Desal. Water Treat., 53 (2015) 794–805.
[35] N. Ma, A. Chen, Z. Bian, Y. Yang, H. Wang, In situ synthesis of a cadmium sulfide/reduced graphene oxide/bismuth Z-scheme oxyiodide system for enhanced photocatalytic performance in chlorinated paraben degradation, Chem. Eng. J., 359 (2019) 530–541.
[36] M. Mahanthappa, N. Kottam, S. Yellappa, Enhanced photocatalytic degradation of methylene blue dye using CuS/CdS nanocomposite under visible light irradiation, Appl. Surf. Sci., 475 (2019) 828–838.
[37] B. Han, S. Liu, Y.-J. Xu, Z.-R. Tang, 1D CdS nanowire–2D $BiVO_4$ nanosheet heterostructures toward photocatalytic selective fine-chemical synthesis, RSC Adv., 5 (2015) 16476–16483.
[38] L. Zou, H. Wang, C. Wu, L. Li, G. Yuan, X. Wang, Construction of all-solid-state Z-scheme 2D $BiVO_4$/Ag/CdS composites with robust photoactivity and stability, Appl. Surf. Sci., 498 (2019) 143900.
[39] N. Clament Sagaya Selvam, Y.G. Kim, D.J. Kim, W.-H. Hong, W. Kim, S.H. Park, W.-K. Jo, Reduced graphene oxide-mediated Z-scheme $BiVO_4$/CdS nanocomposites for boosted photocatalytic decomposition of harmful organic pollutants, Sci. Total Environ., 635 (2018) 741–749.
[40] M. Ohta, S. Hirai, Thermoelectric Properties of $NdGd_{1+x}S_3$ Prepared by CS_2 Sulfurization, J. Electron. Mater., 38 (2009) 1287–1292.
[41] J.B. Gruber, R.P. Leavitt, C.A. Morrison, Absorption spectra, energy levels, and crystal-field analysis of trivalent neodymium in the γ phase of neodymium sesquisulfide (γ-Nd_2S_3), J. Chem. Phys., 79 (1983) 1664–1668.
[42] J.R. Henderson, M. Muramoto, J.B. Gruber, R. Menzel, Optical Spectrum of Single-Crystal Nd_2S_3, J. Chem. Phys., 52 (1970) 2311–2314.
[43] P. Yang, M.K. Lü, C.F. Song, D. Xu, D.L. Yuan, F. Gu, Co-doping effect of CaS and Nd_2S_3 nanocrystallites on luminescence properties of sol–gel SiO_2 xerogel, Mater. Chem. Phys., 91 (2005) 253–256.
[44] S.V. Degtyarev, A.A. Man'shina, A.V. Kurochkin, D.V. Zhuzhel'skii, Y.G. Grigor'ev, Y.S. Tver'yanovich, Glass formation and luminescence of glasses in the Ga_2S_3–GeS_2–Nd_2S_3 system, Glass Phys. Chem., 27 (2001) 209–213.
[45] Y. Xu, M.A.A. Schoonen, The absolute energy positions of conduction and valence bands of selected semiconducting minerals, Am. Mineral., 85 (2000) 543–556.
[46] Z.U. Dzhabua, T.O. Dadiani, A.V. Gigineishvili, M.Y. Stamateli, K.D. Davitadze, G.N. Iluridze, Optical and photoelectric properties of pure and cadmium-and lead-doped neodymium sesquisulfide thin films, Phys. Solid State, 48 (2006) 1481–1485.
[47] D. Lang, Q. Xiang, G. Qiu, X. Feng, F. Liu, Effects of crystalline phase and morphology on the visible light photocatalytic H_2-production activity of CdS nanocrystals, Dalton Trans., 43 (2014) 7245–7253.
[48] D. Tan, W. Fan, W. Xiong, H. Sun, A. Li, W. Deng, C. Meng, Study on adsorption performance of conjugated microporous polymers for hydrogen and organic solvents: the role of pore volume, Eur. Polym. J., 48 (2012) 705–711.
[49] X. Yu, X. An, A. Genç, M. Ibáñez, J. Arbiol, Y. Zhang, A. Cabot, Cu_2ZnSnS_4–PtM (M = Co, Ni) Nanoheterostructures for photocatalytic hydrogen evolution, J. Phys. Chem. C, 119 (2015) 21882–21888.
[50] H. Yang, S.V. Kershaw, Y. Wang, X. Gong, S. Kalytchuk, A.L. Rogach, W.Y. Teoh, Shuttling photoelectrochemical electron transport in tricomponent CdS/rGO/TiO_2 nanocomposites, J. Phys. Chem. C, 117 (2013) 20406–20414.
[51] H. Yang, W. Fan, A. Vaneski, A.S. Susha, W.Y. Teoh, A.L. Rogach, Heterojunction engineering of CdTe and CdSe quantum dots on TiO_2 nanotube arrays: intricate effects of size-dependency and interfacial contact on photoconversion efficiencies, Adv. Funct. Mater., 22 (2012) 2821–2829.